Available online at www.sciencedirect.com
ScienceDirect
Trans. Nonferrous Met. Soc. China 24(2014) 1337−1345
Transactions of Nonferrous Metals Society of China
www.tnmsc.cn

Constitutive behavior, microstructural evolution and processing map of extruded Al−1.1Mn−0.3Mg−0.25RE alloy during hot compression

Tian ZHANG[1], You-rui TAO[1], Xue-yin WANG[2]

1. Mechanical Engineering College, Hunan Institute of Engineering, Xiangtan 411101, China;
2. Golden Dragon Precise Copper Tube Inc., Xinxiang 453000, China

Received 28 May 2013; accepted 20 September 2013

Abstract: Hot compression tests of an extruded Al−1.1Mn−0.3Mg−0.25RE alloy were performed on Gleeble−1500 system in the temperature range of 300−500 °C and strain rate range of 0.01−10 s^{-1}. The associated microstructural evolutions were studied by observation of optical and transmission electron microscopes. The results show that the peak stress level decreases with increasing deformation temperature and decreasing strain rate, which can be represented by a Zener−Hollomon parameter in the hyperbolic-sine equation with the hot deformation activation energy of 186.48 kJ/mol. The steady flow behavior results from dynamic recovery whereas flow softening is associated with dynamic recrystallization and dynamic transformation of constituent particles. The main constituent particles are enriched rare earth phases. Positive purifying effects on impurity elements of Fe and Si are shown in the Al−1.1Mn−0.3Mg−0.25RE alloy, which increases the workability at high temperature. Processing map was calculated and an optimum processing was determined with deformation temperature of 440−450 °C and strain rate of 0.01 s^{-1}.
Key words: Al−1.1Mn−0.3Mg−0.25RE alloy; flow stress; constitutive behavior; microstructural characterization; processing map

1 Introduction

There is a growing demand for more fuel-efficient vehicles to reduce energy consumption and air pollution for the automotive industry [1]. The Al−Mn system alloys are traditionally processed into sheet and extruded products which are widely used for automotive heat exchangers due to their combined performance of strength, formability, brazeability, and corrosion resistance. Recently, numbers of efforts, i.e., by adding or improving alloy element compositions or optimizing processing schedule, have been made to improve the corrosion resistance and mechanical performance to meet the increased challenges of the reduction in thickness of tube and fin products [2,3].

Rare earth (RE) elements have shown beneficial effects on melting and solidification in conventionally cast aluminum alloys. Such micro-alloying elements reduce the contents of gases, some impurities and the spacing between secondary dendrite arms, which have been studied for several years in aluminum alloys. It was reported that Ce addition affected the grain size, mechanical property, ductility and fracture toughness of various aluminum alloys rich in impurities of Fe, Si and alkali metals [4−9]. MENG et al [5,6] reported that the Ce content affected the grain size of a binary Al−Li alloy and the mechanical properties of Al−Li−Mg alloys containing impurity Fe. The number of grains per unit area in the binary alloy linearly increases with raising the Ce content up to 1.1%. The mechanical properties of the cast Al−Li−Mg alloys were improved and the negative effect of impurity Fe was controlled by Ce content. Recent works also showed that Ce addition could increase the density and thermal stability of fine Ω precipitates [7] and promote the precipitation of denser and finer θ' phase [8], which resulted in improved mechanical properties. DAUD et al [9] found that both the paint bake hardness and peak hardness were increased by the addition of Ce in Al−0.5Mg−1.2Si−0.25Fe alloy, which is related to grain refinement and formation of precipitates, and then led to improvement of the dent resistance. The precipitation kinetics of Ω phase was distinctly retarded by promoting the formation of θ'

Foundation item: Project (31115014) supported by the of Open Research Fund Program of State Key Laboratory of Advanced Design and Manufacture for Vehicle Body (Hunan University); Project (12JJ9017) supported by the Natural Science Foundation of Hunan Province, China
Corresponding author: You-rui TAO; Tel: +86-731-58688521; E-mail: yr.tao@126.com
DOI: 10.1016/S1003-6326(14)63197-6

phase, but the fatigue crack propagation resistance was significantly enhanced and the dendritic substructure of as-cast alloy was refined remarkably in the Er-containing Al−Cu−Mg−Ag alloy [10]. By adding RE elements to Al−Mn alloy, we have developed a new high corrosion resistance and mechanical performance Al−Mn alloy, which is Al−1.1Mn−0.3Mg−0.25RE alloy.

Another effective way to promote the quality of Al−Mn alloy products is to optimize the processing schedule and hot deformation is a key manufacturing process. Therefore, designing and developing new tube or sheet alloys with improved properties require a detailed understanding of the hot deformation mechanisms of these new alloys [11,12]. While little work has been done in hot deformation mechanisms of such new developed alloys. In the present work, the hot compression tests of a new designed extruded Al−1.1Mn−0.3Mg−0.25RE alloy are to be performed on Gleeble−1500 machine at strain rate ranging between 0.01−10 s^{-1} and deformation temperature of 300−500 °C. The purpose is to gain a fundamental understanding of the hot deformation behavior of Al−1.1Mn−0.3Mg−0.25RE alloy, including the effects of thermo-mechanical parameters and rare earth elements on the flow stress and microstructural evolutions during hot compression.

2 Experimental

The experiments were carried out on an Al−1.1Mn−0.3Mg−0.25RE alloy. Cylindrical samples, with 10 mm in diameter and 15 mm in height, were machined from a bar (10 mm in diameter) which was extruded from a cylindrical cast ingot (80 mm in diameter and 300 mm in length). And then convex depressions of 0.2 mm depth were machined on both ends of the samples in order to maintain the lubricant of graphite mixed with machine oil during compression tests. Isothermal compression tests were carried out on a computer servo-controlled Gleeble−1500 system in strain rate range of 0.01−10 s^{-1} and in deformation temperature range of 300−500 °C, with the specific true strain of 0.8. The sample was resistance heated to deformation temperature at a heating rate of 10 °C/s and held at that temperature for 180 s by thermo-coupled-feedback-controlled AC current before compression, and then the samples were deformed to half of their original height and water quenched immediately. The deformed samples were sectioned parallel to the compression axis along the direction of centerline and prepared by the conventional methods for the microstructural observations on an Axiovert 40 MAT metallographic microscope (OM) after etching by mixed enchants (1.0 mL HF+1.5 mL HCl+2.5 mL HNO_3+95 mL H_2O) for 30 s. The thin samples were examined on a JEM3010 transmission electron microscope (TEM) after electropolishing in a solution of 30% HNO_3 and 70% methanol at 25 V and −30 °C.

3 Results and discussion

3.1 Flow stress and constitutive equations

The true stress−true strain curves of the extruded Al−1.1Mn−0.3Mg−0.25RE alloy deformed in strain rate range of 0.01−10 s^{-1} and temperature range of 300−500 °C are given in Fig. 1. Significant effects of deformation parameters (including strain, temperature and strain rate) on the flow stress behavior are presented. The flow stress increases with increasing strain and tends to be steady after a peak value, showing a steady state flow until the end of deformation. But when deformed below 450 °C and at high strain rates, the flow stress reaches a plateau and then increases slightly until high strains, showing a flow hardening, which little agrees with several reported aluminum alloys [12−15]. The peak stress values increase with increasing strain rate and decreasing deformation temperature. And because of the different rapid hardening rate at initial deformation stages, the strain corresponding to the peak stress increases with increasing strain rate and with decreasing deformation temperature. The rapid rise in flow stress was due to the work hardening at the onset of the deformation. And the formation of tangled dislocation structures, as barriers to the dislocation movement, is believed to be the reason for the observed flow behavior. The steady flow behavior is probably subjected to the dynamic recovery (DRV) and dynamic recrystallization (DRX) during hot deformation of the non-heat-treatable aluminum alloys [16−18]. The actual hot deformation mechanisms for the studied alloy will be discussed in detail in the following section by comparison with hot deformation activation energy calculation, microstructural observation and processing maps.

Generally, the following constitutive equations are applied in hot deformation to describing the effects of deformation conditions on the state of flow stress [19−21]:

$$Z = f_1(\sigma) = A_1\sigma^{n_1} \quad (1)$$

$$Z = f_2(\sigma) = A_2\exp(\beta\sigma) \quad (2)$$

where A_1, A_2, n_1 and β are constants; σ is the peak stress or steady state stress; Z is the Zener−Hollomon parameter which can be expressed as follows:

$$Z = \dot{\varepsilon}\exp\left(\frac{Q}{RT}\right) \quad (3)$$

where $\dot{\varepsilon}$ is the strain rate; T is the deformation temperature; Q is an activation energy for hot deformation; R is the gas constant (8.314 J/(mol·K^{-1})).

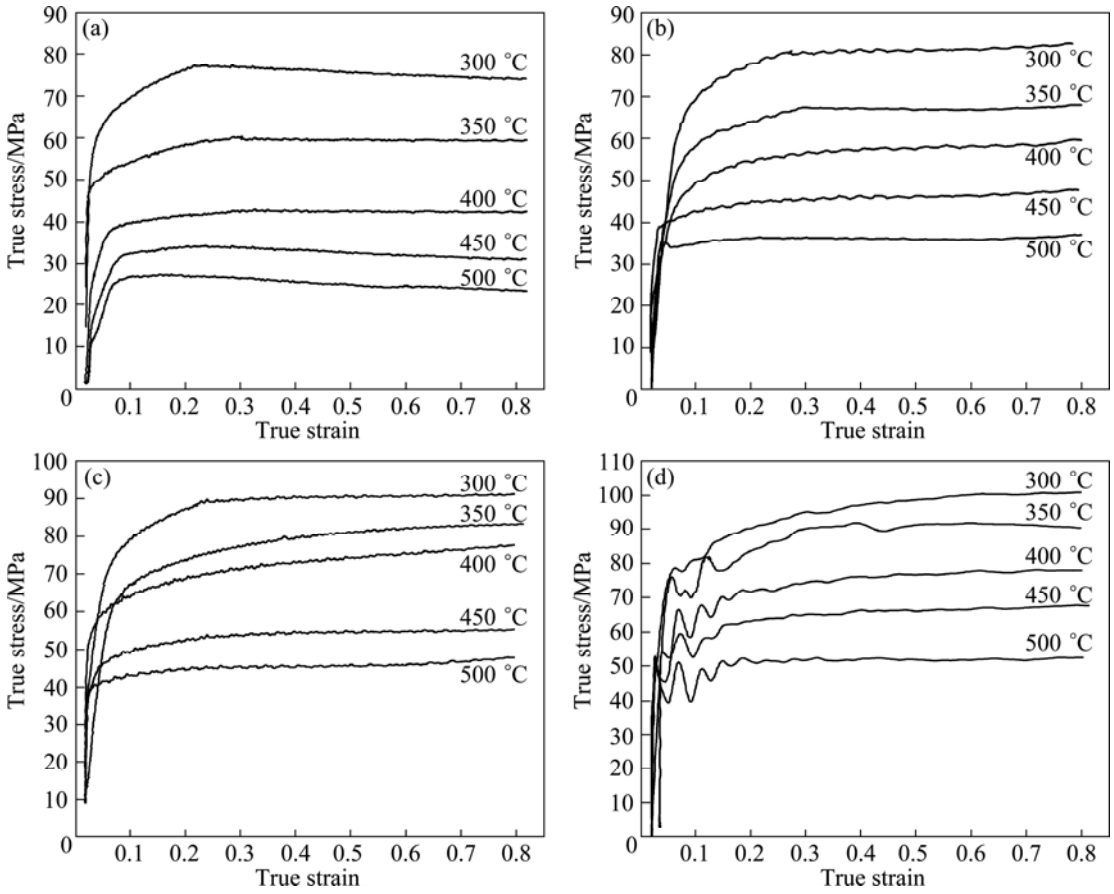

Fig. 1 True stress−true strain curves of Al−1.1Mn−0.3Mg−0.25RE alloy during hot compression deformation: (a) $\dot{\varepsilon}$=0.01 s^{-1}; (b) $\dot{\varepsilon}$=0.1 s^{-1}; (c) $\dot{\varepsilon}$=1 s^{-1}; (d) $\dot{\varepsilon}$=10 s^{-1}

The power law (Eq. (1)) and the exponent-type equation (Eq. (2)) break at a high stress and at a low stress, respectively. The hyperbolic-sine equation (Eq. (4)), proposed by SELLARS and McTEGERT [22], is a more suitable equation over a wide range to describe the flow stress.

$$Z = f(\sigma) = A(\sinh \alpha\sigma)^n \quad (4)$$

where A and n are constants; α is the stress multiplier, also the additional adjustable parameter.

The flow stress is a function of deformation temperature and strain rate which is expressed in above equations. The combined effects of temperature and strain rate on the flow stress could be expressed by Z (Eq. (4)). In the present work, the flow stress reached a peak value and almost remained constant thereafter for most samples. Therefore, the peak values were used to model the hot deformation behavior of powder compacts and the effect of strain on the flow stress would not be considered. The values of n_1 or n and β can be obtained by means of linear regression through Eq. (1) and Eq. (2), respectively. Then an estimated value of α was taken as a first approximation and a new value of n can be obtained by deriving Eq. (4), and then iterated to obtain the optimum values of α, n, A and Q [15, 23, 24]. The linear relationships of $\ln\dot{\varepsilon} - \ln[\sinh(\alpha\sigma)]$ and $\ln[\sinh(\alpha\sigma)] - 1000/T$ are obtained in Fig. 2, and then the values of material constants of the present alloy can be obtained from the experimental data and are shown in Table 1. Such parameters can be used for describing the quantificational relationships of the flow stress and temperature and strain rate by the Zener−Hollomon parameter in the hyperbolic-sine equation with related coefficient of 0.97.

The physical parameter Q is usually served as an indicator of deformation difficulty degree in plasticity deformation. The value of Q for the studied alloy is 186.48 kJ/mol, which is much higher than that of the previous 3003 aluminum alloy (164.8 kJ/mol) [20] and Al−1Mn alloy (152 kJ/mol) [25]. The higher Q value may be attributed to the combined influence of work hardening after extruding and grain refining by the addition of rare earth elements [6,9,10].

3.2 Microstructural evolution

Typical optical microstructures developed with ln Z values during hot deformation are presented in Fig. 3. The original grain boundaries of lamellar columnar or

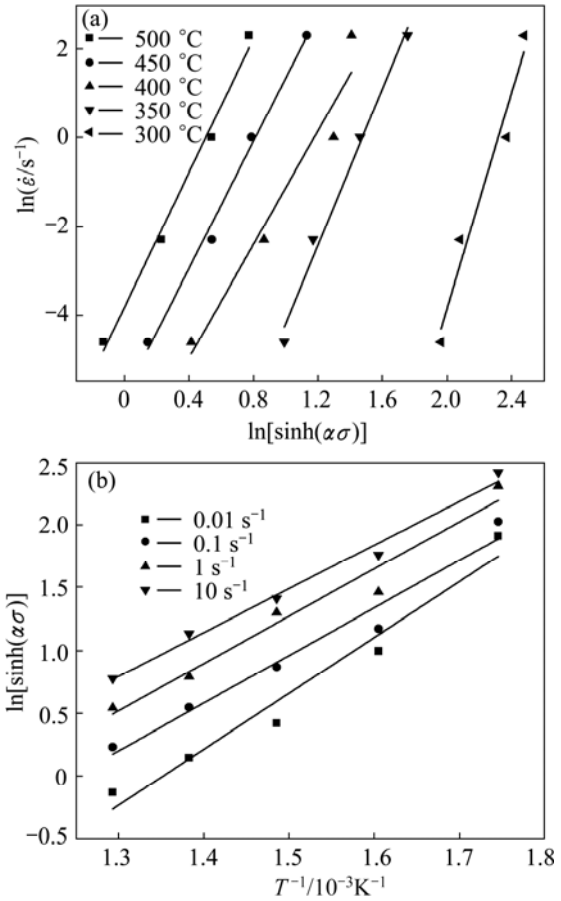

Fig. 2 Linear relationships of various parameters: (a) Peak flow stress as function of strain rate; (b) Plot used for estimating Q

Table 1 Material constants of Al−1.1Mn−0.3Mg−0.25RE alloy used in hyperbolic-sine equation

A/s^{-1}	α/MPa^{-1}	n	Q/(kJ·mol^{-1})
1.07697×10^{10}	0.037403	5.875667	186.48

elongated grains, roughly parallel to extrusion axis and compression direction, are gradually serrated by compression with decreasing ln Z value which is combined with the deformation temperature and strain rate. With decreasing ln Z value, seen in Figs. 3(c) and (d), serrated grain boundaries occur between the original serrated grain boundaries. These grain boundaries come in touch with each other with visible protrusions, leading to transformation of new grains and exhibiting serrations with sizes approximately equal to the width of the original columnar grain. A process of serration is so strong that grain protrusions develop, finally pinch off from the grain to become isolated new grains (Fig. 3 (d)), which shows a typical grain structure developed by geometric dynamic recrystallization (GDRX) [18,25,26]. The serrations become more prominent as the temperature rises and strain rate diminishes, while their wavelength depends on subgrain sizes [27].

A series of TEM images of the specimens deformed at different temperatures and strain rates are shown in Fig. 4. Substructure is one of the most important structural features directly related to the deformation processing. The substructure is not well formed with low-angle boundaries and exhibits a high dislocation

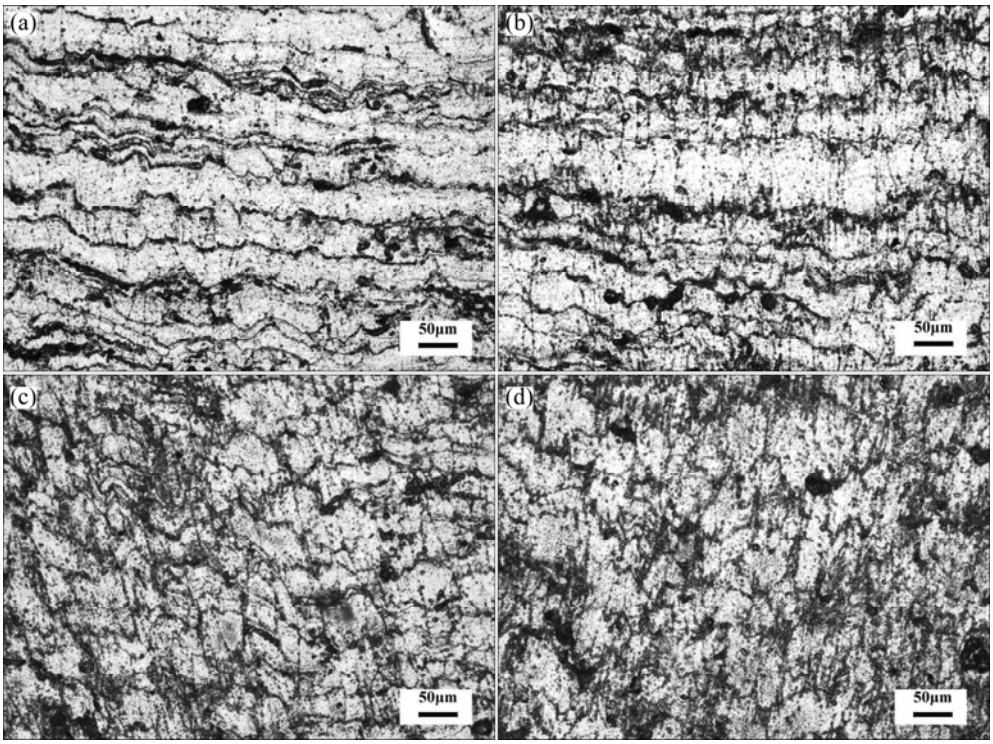

Fig. 3 Optical microstructures of Al−1.1Mn−0.3Mg−0.25RE alloy deformed at various conditions: (a) ln Z=38.32 (t=350 °C, $\dot{\varepsilon}$=10 s^{-1}); (b) ln Z=33.34 (t=400 °C, $\dot{\varepsilon}$=1 s^{-1}); (c) ln Z=28.74 (t=450 °C, $\dot{\varepsilon}$=0.1 s^{-1}); (d) ln Z=24.43 (t=500 °C, $\dot{\varepsilon}$=0.01 s^{-1})

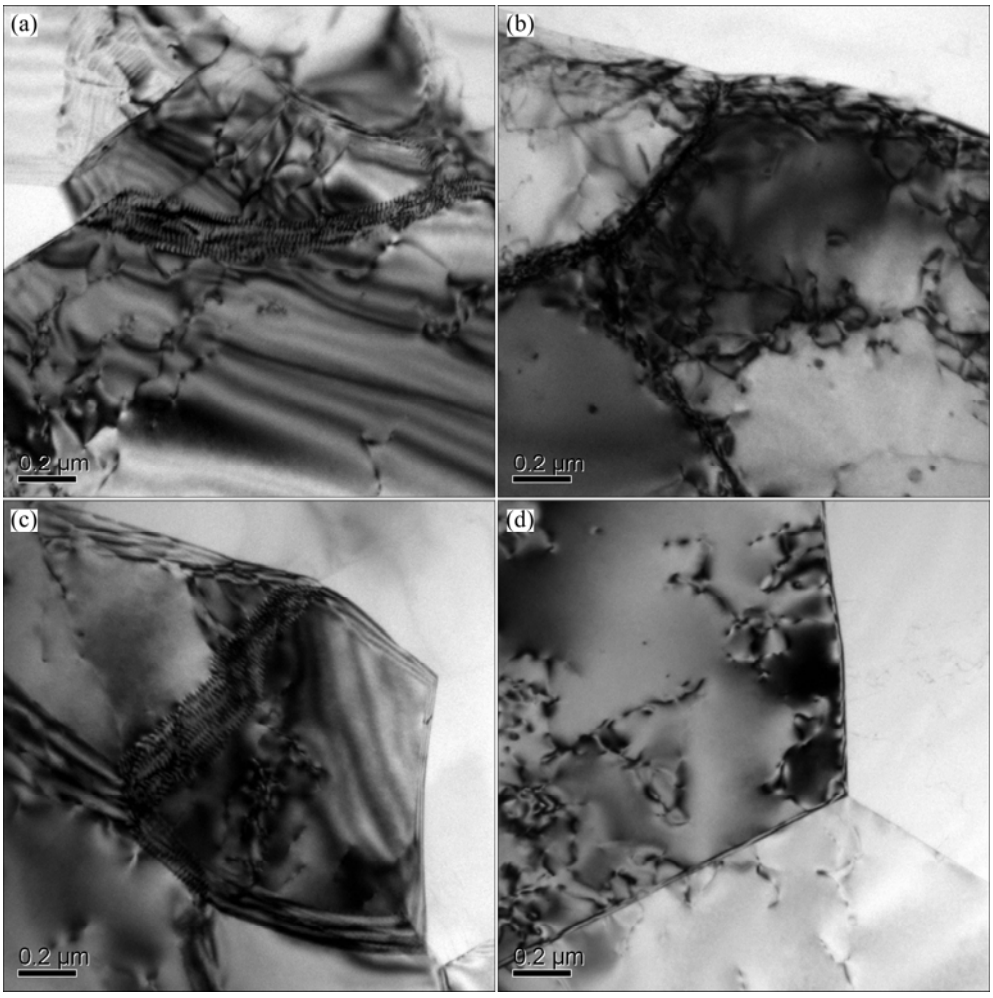

Fig. 4 TEM images showing subgrains of Al−1.1Mn−0.3Mg−0.25RE alloy deformed at different conditions: (a) ln Z=38.32 (t=350 °C, $\dot{\varepsilon}$=10 s^{-1}); (b) ln Z=33.34 (t=400 °C, $\dot{\varepsilon}$=1 s^{-1}); (c) ln Z=28.74 (t=450 °C, $\dot{\varepsilon}$=0.1 s^{-1}); (d) ln Z=24.43 (t=500 °C, $\dot{\varepsilon}$=0.01 s^{-1})

density with poorly developed cellularity for the specimen deformed at temperature of 350 °C and strain rate of 10 s^{-1}, which presents a typical high Z value deformation (shown in Fig. 4(a)). The sub-boundary definitions become more indistinct owing to the dislocation tangles. On the contrary, when the specimen is deformed at lower Z, as shown in Figs. 4(b)−(d), especially at temperature of 500 °C and strain rate of 0.01 s^{-1}, the subgrain size increases with increasing deformation temperature or decreasing strain rate, while sub-boundary changes from low angle to high angle. The sufficient migrations of atoms and dislocations cause the merging of some subgrains, and low-angle grain boundaries transform into high-angle grain boundaries through absorbing dislocations [16,17]. All of these will result in lower density of dislocations and high-angle subgrain boundaries at lower Z value finally (Fig. 4 (d)).

Figure 5 shows TEM images of constituent particles, which indicates that dynamic transformation of constituent particles has occurred with various Z values. It can be seen that the morphology of particles changes from coarse rod-like to fine round with an increase in density when decreasing Z value, which will provide more nuclear sites for dynamic recrystallization and improve the workability by releasing stress concentration at the corner of particles. There is an enhanced driving force partial dissolution of constituent particles with decreasing Z values, which is induced by the partial pure shear deformation favorable for the accumulation of substructure and strain energy [28] and the high temperature [29]. Combining the electron diffraction pattern and the results of energy dispersive spectrometry (EDS) analysis (Table 2), the main constituent particles are enriched rare earth phases (Al_2RE) with FCC crystal structure. The EDS results show that Fe and Si are gradually dissolved into enriched rare earth particles with decreasing Z value. The appearance of Al−RE−Si ternary phase (Figs. 5(b, c)) and Al−RE−Si−Fe phase (Fig. 5(d)) agrees well with positive purifying effects on impurity elements of Fe and Si, which will improve the

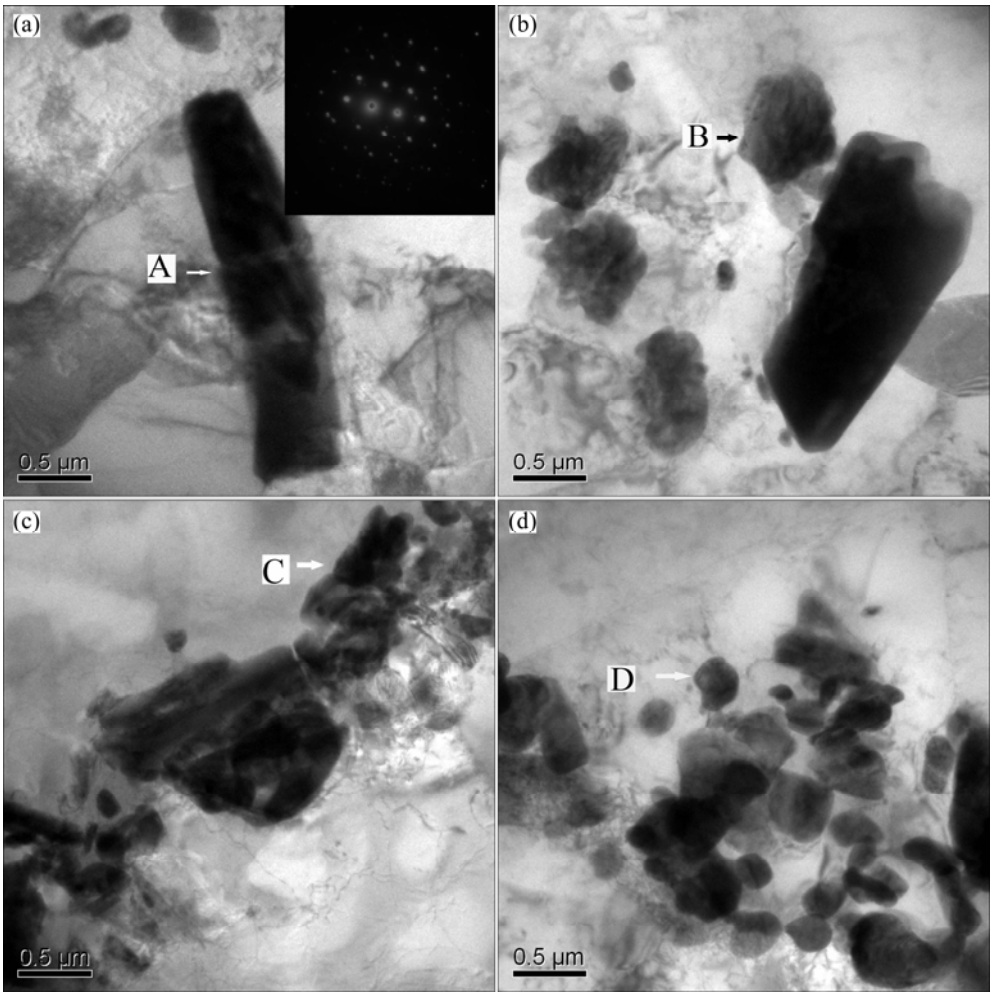

Fig. 5 TEM images showing presence of constituent particles of Al−1.1Mn−0.3Mg−0.25RE alloy deformed at different conditions: (a) ln Z=38.32 (t=350 °C, $\dot{\varepsilon}$=10 s^{-1}); (b) ln Z=33.34 (t=400 °C, $\dot{\varepsilon}$=1 s^{-1}); (c) ln Z=28.74 (t=450 °C, $\dot{\varepsilon}$=0.1 s^{-1}); (d) ln Z=24.43 (t=500 °C, $\dot{\varepsilon}$=0.01 s^{-1})

Table 2 Chemical compositions of constituent particles of Al−1.1Mn−0.3Mg−0.25RE alloy analyzed by EDS in Fig. 5

Label	w(Si)/%	w(Fe)/%	w(Ce)/%	w(La)/%	w(Al)/%
A	−	−	23.66	−	Bal.
B	5.19	−	55.36	15.40	Bal.
C	5.86	−	49.61	14.20	Bal.
D	0.67	0.47	34.46	14.04	Bal.

ductility and toughness of the alloys [6−8]. MENG et al [5,6] suggested that the amount of rare earth elements might suppress the detrimental effects of impurities on mechanical properties of Al−Li alloys because the actions of rare earth elements on the microstructure are opposite from those of the deleterious impurities and rare earth elements produce possibly dragging effect on impurity atom segregation to grain boundaries.

3.3 Processing map

Processing maps are widely used to optimize the processing parameters in hot working of aluminum alloys, which are plotted based on the dynamic materials modeling (DMM) and consider the workpiece as a power. The power dissipation rate is given by a dimensionless parameter, called the efficiency of power dissipation (η), =2m/(m+1), where m is the strain rate sensitivity of flow stress [30]. The parameter η describes the constitutive response of the work-piece in terms of various microstructural mechanisms that operate in a given regime of deformation temperature and strain rate. The evolutions of η with temperature and strain rate constitute a power dissipation map exhibiting different domains, which may be directly correlated with specific microstructure. The optimal hot deformation mechanisms are DRV, DRX and superplasticity, while wedge cracking and void formation at hard particles are damaged processes. Acicular perform structures deformed at an elevated temperature exhibit the process of spheroidization, which occurs in the shearing of the lamellae and globularization, and is considered to be a

type of DRX [31].

A continuous instability criterion based on extremism principles of irreversible thermodynamics applied to large plastic flow is used to identify the regime of flow instabilities. In terms of the maximum rate of entropy production in material system, an instability criterion could be derived by following equation [30−32]:

$$\xi(\dot{\varepsilon}) = \frac{\partial \ln[m/(m+1)]}{\partial \ln \dot{\varepsilon}} + m < 0 \quad (6)$$

The evolutions of dimensionless parameter $\xi(\dot{\varepsilon})$ with deformation temperature and strain rate constitute an instability map. The data of $\ln \sigma$ vs $\ln \dot{\varepsilon}$ are fitted using a cubic spline function at a strain, and the strain rate sensitivity is evaluated as a function of strain rate, which is repeated at different deformation temperatures. In order to obtain the power dissipation map and instability map, the power dissipation efficiency and the dimensionless instability parameter are calculated from a series of m-values. Finally, the processing map is obtained by superimposing the instability map on the power dissipation map [30,31].

Figure 6 shows the power dissipation map and processing map during hot compression of Al−1.1Mn−0.3Mg−0.25RE alloy constructed at deformation temperatures ranging from 300 °C to 500 °C and strain rate ranging from 0.01 s^{-1} to 10 s^{-1} at strain of 0.7. The dashed areas represent flow instability domains while non-dashed areas are reasonable deformation domains, as shown in Fig. 6(b). Large scale of instability domains are presented both at low and high temperatures, which means nearly little reasonable deformation domains appear at temperatures ranging from 300 °C to 420 °C, and limited reasonable deformation domains (strain rate between 0.1 $s^{-1}$and 1 s^{-1}) arise at temperatures ranging from 470 °C to 500 °C. The values of power dissipation increase with decreasing strain rate or increasing deformation temperature (Fig. 6(a)). Generally, the optimal deformation domain is associated with higher η in processing map which represents special microstructural mechanisms such as DRV or DRX [30,31]. Typical optical microstructures corresponding to instability domains and deformation domains with decreasing Z values are given in Fig. 7. It can be seen that serrated grain boundaries occur between the original

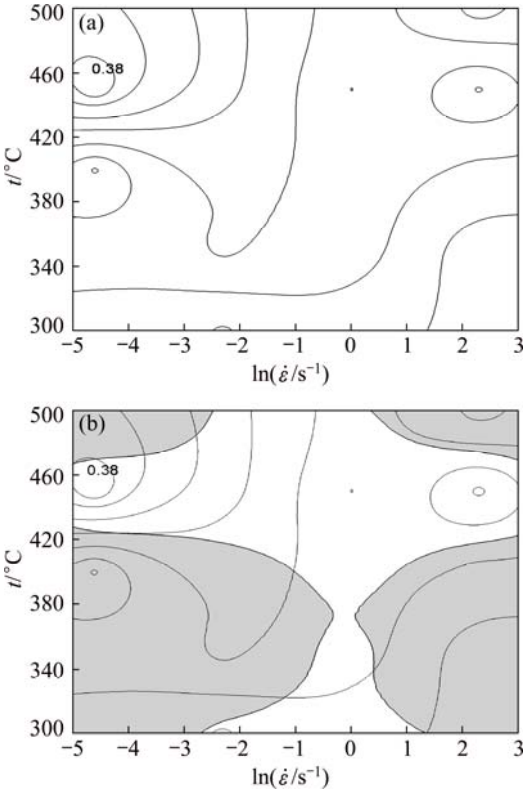

Fig. 6 Power dissipation map (a) and processing map (b) of Al−1.1Mn−0.3Mg−0.25RE alloy at strain of 0.7

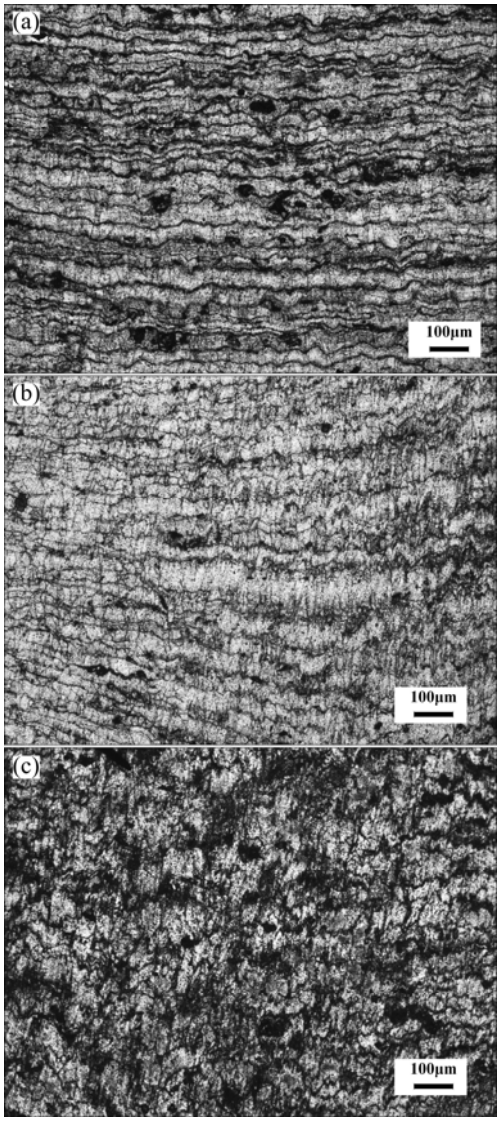

Fig. 7 Optical microstructures of Al−1.1Mn−0.3Mg−0.25RE alloy deformed different conditions: (a) t=350 °C, $\dot{\varepsilon}$=10 s^{-1}: (b) t=400 °C, $\dot{\varepsilon}$=0.01 s^{-1}; (c) t=500 °C, $\dot{\varepsilon}$=0.01 s^{-1}

elongated grain boundaries at temperature of 400 °C and strain rate of 0.01 s^{-1}, which present GDRX and lead to stable flow state and improved workability [31,32]. However, serrated grain boundaries with little DRX grains are shown at temperature of 350 °C and strain rate of 10 s^{-1}, and coarse DRX grains are shown at temperature of 500 °C and strain rate of 0.01 s^{-1}. Hence, an optimum processing is determined primarily with deformation temperature of 440−450 °C and strain rate of 0.01 s^{-1}.

4 Conclusions

1) The flow stress increases sharply with increasing strain initially and then tends to be constant after a peak value, showing a steady state flow until high strains. The peak stress level decreases with increasing deformation temperature and decreasing strain rate, which can be represented by a Zener−Hollomon parameter in the hyperbolic-sine equation with the hot deformation activation energy of 186.48 kJ/mol.

2) The steady state flow results from dynamic recovery whereas flow softening is associated with dynamic recrystallization and dynamic transformation of constituent particles. The main enriched rare earth constituent particles and the positive purifying effects on impurity elements of Fe and Si in the Al−1.1Mn−0.3Mg−0.25RE alloy are demonstrated. And the workability of the alloy is improved with decreasing Z value (especially at high temperature) due to refined and spheroidized particles.

3) The processing maps were calculated and an optimum processing was determined with deformation temperature of 440−450 °C and strain rate of 0.01 s^{-1}.

References

[1] MILLER W S, ZHUANG L, BOTTEMA J, WITTEBROOD A J, SMET P D, HASZLER A, VIEREGGE A. Recent development in aluminium alloys for the automotive industry [J]. Materials Science and Engineering A, 2000, 280: 37−39.

[2] VENKATESWRLU K, MURTY B S, CHAKRABORTY M. Effect of hot rolling and heat treatment of Al−5Ti−1B master alloy on the grain refining efficiency of aluminium [J]. Materials Science and Engineering A, 2001, 301: 180−186.

[3] ALEXANDER D T L, GREER A L. Solid-state intermetallic phase transformations in 3xxx aluminium alloys [J]. Acta Materialia, 2002, 50: 2571−2583.

[4] POLMEAR I J. A trace element effect in alloys based on the aluminium−zinc−magnesium system [J]. Nature, 1960, 186: 303−304.

[5] MENG Liang, ZHENG Xiu-lin, TIAN Li. Effect of alkali metal impurities and cerium modification on the fatigue behaviour of 8090 alloy sheets [J]. Materials Science and Engineering A, 1995, 196: 191−196.

[6] MENG Liang, ZHENG Xiu-lin. Overview of the effects of impurities and rare earth elements in A1−Li alloys [J]. Materials Science and Engineering A, 1997, 237: 109−118.

[7] XIAO D H, WANG J N, DING D Y, YANG H L. Effect of rare earth Ce addition on the microstructure and mechanical properties of an Al−Cu−Mg−Ag alloy [J]. Journal of Alloys and Compounds, 2003, 352: 84−88.

[8] WANG Wen-tao, ZHANG Xin-ming, GAO Zhi-guo, JIA Yu-zhen, YE Ling-ying, ZHENG Da-wei, LIU Ling. Influences of Ce addition on the microstructures and mechanical properties of 2519A aluminum alloy plate [J]. Journal of Alloys and Compounds, 2010, 491: 366−371.

[9] DAUD A R, WONG K M C. The effect of cerium additions on dent resistance of Al−0.5Mg−1.2Si−0.25Fe alloy for automotive body sheets [J]. Materials Letters, 2004, 58: 2545−2547.

[10] BAI Song, LIU Zhi-yi, LI Yun-tao, HOU Yan-hui, CHEN Xu. Microstructures and fatigue fracture behavior of an Al−Cu−Mg−Ag alloy with addition of rare earth Er [J]. Materials Science and Engineering A, 2010, 527: 1806−1814.

[11] MARTINS J P, CARVALHO A L M, PADILHA A F. Microstructure and texture assessment of Al−Mn−Fe−Si (3003) aluminum alloy produced by continuous and semicontinuous casting processes [J]. Journal of Materials Science, 2009, 44: 2966−2976.

[12] ZHANG Hui, JIANG Fu-lin, SHANG Xiao-yang, LI Luo-xing. Flow stress and microstructural evolution of the horizontal continuous casting Al−0.96Mn−0.38Si−0.18Fe alloy during hot compression [J]. Materials Science and Engineering A, 2013, 571: 25−32.

[13] CERRI E, EVANGELISTA E, FORCELLESE A, MCQUEEN H J. Comparative hot workability of 7012 and 7075 alloys after different pretreatments [J]. Materials Science and Engineering A, 1995, 197: 181−198.

[14] GAVGALI M, AKSAKAL B. Effects of various homogenisation treatments on the hot workability of ingot aluminium alloy AA2014 [J]. Materials Science and Engineering A, 1998, 254: 189−199.

[15] ZHANG Hui, LI Luo-xing, YUAN Deng, PENG Da-shu. Hot deformation behavior of the new Al−Mg−Si−Cu aluminum alloy during compression at elevated temperatures [J]. Materials Characterization, 2007, 58: 168−173.

[16] GLEZ J C, DRIVER J H, Substructure development in hot plane strain compressed Al−1%Mn crystals [J]. Acta Materialia, 2003, 51: 2989−3003.

[17] FURU F, ORSUND R, NES E. Substructure evolution during different hot deformation processes of commercial non-heat treatable aluminium alloys [J]. Materials Science and Engineering A, 1996, 214: 122−132.

[18] DOHERTY R D, HUGHES D A, HUMPHREYS F J, JONAS J J, JENSEN D J, KASSNER M E, KING W E, MCNELLEY T R, McQUEEN H J, ROLLETT A D. Current issues in recrystallization: a review [J]. Materials Science and Engineering A, 1997, 238: 219−274.

[19] McQUEEN H J, RYAN N D. Constitutive analysis in hot working [J]. Materials Science and Engineering A, 2002, 322: 43−63.

[20] SHEPPARD T, JACKSON A. Constitutive equations for use in prediction of flow stress during extrusion of aluminum alloys [J]. Materials Science and Technology, 1997, 13: 203−209.

[21] ZENER C, HOLLOMON J H. Effect of strain-rate upon the plastic flow of steel [J]. Journal of Applied Physics, 1944, 15: 22−27.

[22] SELLARS C M, MCTEGERT W J. On the mechanism of hot deformation [J]. Acta Materialia, 1966, 14: 1136−1138.

[23] TALEGHANI M A J, NAYAS E M R, SALEHI M, TORRALBA J M. Hot deformation behaviour and flow stress prediction of 7075 aluminium alloy powder compacts during compression at elevated temperatures [J]. Materials Science and Engineering A, 2012, 534: 624−631.

[24] LIN Yong-cheng, LI Qi-fei, XIA Yu-chi, LI Lei-ting. A phenomenological constitutive model for high temperature flow

stress prediction of Al−Cu−Mg alloy [J]. Materials Science and Engineering A, 2012, 534: 654−662.
[25] ZHANG H, KONOPLEVA E V, MCQUEEN H J. Effects of Mn dispersoid on hot working of Al−1Mn [J]. Materials Science and Engineering A, 2001, 319−321: 711−715.
[26] BLUM W, ZHU Q, MERKEL R, McQUEEN H J. Geometric dynamic recrystallization in hot torsion of Al−5Mg−0.6Mn (AA5083) [J]. Materials Science and Engineering A, 1996, 205: 23−30.
[27] KONOPLEVA E V, MCQUEEN H J, EVANGELISTA E. Serrated grain boundaries in hot-worked aluminum alloys at high strains [J]. Materials Characterization, 1995, 34: 251−264.
[28] LIU Zhi-yi, CHEN Xu, HAN Xiang-nan, GU Yan-xia. The dissolution behavior of θ' phase in Al−Cu binary alloy during equal channel angular pressing and multi-axial compression [J]. Materials Science and Engineering A, 2010, 527: 4300−4305.
[29] CABIBBO M. Partial dissolution of strengthening particles induced by equal channel angular pressing in an Al−Li−Cu alloy [J]. Materials Characterization, 2012, 68: 7−13.
[30] PRASAD Y V R K, GEGEL H L, DORAIVELU S M, MALAS J C, MORGAN J T, LARK K A, BARKER D R. Modeling of dynamic material behavior in hot deformation: Forging of Ti-6242 [J]. Metallurgical Transactions A, 1984, 15: 1883−1892.
[31] PRASAD Y V R K, SESHACHARYULU T. Processing maps for hot working of titanium alloys [J]. Materials Science and Engineering A, 1998, 243: 82−88.
[32] LUO J, LI M Q, MA D W. The deformation behavior and processing maps in the isothermal compression of 7A09 aluminum alloy [J]. Materials Science and Engineering A, 2012, 532: 548−557.

挤压态 Al−1.1Mn−0.3Mg−0.25RE 合金热变形本构特性、显微组织演变及加工图

张 添[1]，陶友瑞[1]，王学印[2]

1. 湖南工程学院 机械工程学院，湘潭 411101；
2. 金龙精密铜管集团股份有限公司，新乡 453000

摘 要：在 Gleeble−1500 热模拟机上对 Al−1.1Mn−0.3Mg−0.25RE 合金在变形温度 300~500 °C 和应变速率 0.01~10 s^{-1} 条件下进行高温热压缩实验，并采用光学金相显微镜及透射电镜对该合金热变形过程的显微组织演变规律进行观察。结果表明：Al−1.1Mn−0.3Mg−0.25RE 合金的峰值应力随着变形温度的升高而减小，随着应变速率的增大而增大，并可用包含 Zener−Hollomon 参数的双曲正弦关系来描述合金的热流变行为，其变形激活能为 186.48 kJ/mol；热变形过程稳流过程是动态回复引起的，而流变软化与动态再结晶及成分相的转变有关；合金中主要成分相是富稀土相，这些相的形成对 Fe 和 Si 等杂质元素具有净化作用，并增加该合金在高温条件下的热加工性。结合加工图和显微组织可以确定在该实验范围内，合金热变形的最佳工艺参数为：热加工温度 440~450 °C，应变速率 0.01 s^{-1}。

关键词：Al−1.1Mn−0.3Mg−0.25RE 合金；流变应力；本构模型；显微组织；加工图

(Edited by Hua YANG)